

# Deep learning of dynamical attractors from time series measurements

William Gilpin<sup>1</sup>

## Abstract

Experimental measurements of physical systems often have a finite number of independent channels, causing essential dynamical variables to remain unobserved. However, many popular methods for unsupervised inference of latent dynamics from experimental data implicitly assume that the measurements have higher intrinsic dimensionality than the underlying system—making coordinate identification a dimensionality reduction problem. Here, we study the opposite limit, in which hidden governing coordinates must be inferred from only a low-dimensional time series of measurements. Inspired by classical techniques for studying the strange attractors of chaotic systems, we introduce a general embedding technique for time series, consisting of an autoencoder trained with a novel latent-space loss function. We first apply our technique to a variety of synthetic and real-world datasets with known strange attractors, and we use established and novel measures of attractor fidelity to show that our method successfully reconstructs attractors better than existing techniques. We then use our technique to discover dynamical attractors in datasets ranging from patient electrocardiograms, to household electricity usage, to eruptions of the Old Faithful geyser—demonstrating diverse applications of our technique for exploratory data analysis.

## 1. Introduction

Unsupervised learning has recently been applied to the problem of discovering dynamical models directly from experimental data. Given high-dimensional observations of an experimental dataset, neural networks can readily extract latent coordinates, which can either be time-evolved through empirical time-evolution operators or fit directly to differential equations (Champion et al., 2019; Sun et al., 2019;

Takeishi et al., 2017; Linderman et al., 2017; Otto & Rowley, 2019). This process represents an empirical analogue of the traditional model-building approach of physics, in which approximate mean-field or coarse-grained dynamical variables are first inferred from first principles, and then used as independent coordinates in a reduced-order model (Bar-Sinai et al., 2019). However, many such techniques implicitly assume that the degrees of freedom in the raw data span the system’s full dynamics, making dynamical inference a dimensionality reduction problem.

Here, we study the inverse problem: given a single, time-resolved measurement of a complex dynamical system, is it possible to reconstruct the higher-dimensional process driving the dynamics? This process, known as state space reconstruction, is the focus of many classical results in nonlinear dynamics theory, which has demonstrated various heuristics for reconstructing effective coordinates from the time history of the system (Kennel et al., 1992; Abarbanel et al., 1993). Such techniques have broad application throughout the natural sciences, particularly in areas in which simultaneous multidimensional measurements are difficult to obtain—such as ecology, electrophysiology, and climate science (Deyle & Sugihara, 2011; Clark & Luis, 2020). However, these embedding techniques are strongly sensitive to hyperparameter choice, system dimensionality, non-stationarity, and experimental measurement error—therefore requiring extensive tuning and in-sample cross-validation before they can be applied to a new dataset (Cobey & Baskerville, 2016). Additionally, current methods cannot consistently infer the underlying dimensionality as the original system—making them prone to redundancy and overfitting (Pecora et al., 2007). Several of these shortcomings may be addressable by revisiting these classical techniques in the context of recent advances in machine learning, motivating our study.

**Overview and Contributions.** Our goal is to develop a general-purpose method for reconstructing the  $d$ -dimensional attractor of an unknown dynamical system, given only a univariate measurement time series.

- We introduce a custom loss function and regularizer for autoencoders, the false-nearest-neighbor loss, that allows multiple autoencoder architectures to successfully reconstruct unseen dynamical variables from univariate time series.

<sup>1</sup>NSF-Simons Center for Mathematical & Statistical Analysis of Biology, Harvard University, Cambridge, MA. Correspondence to: William Gilpin <wgilpin@fas.harvard.edu>.

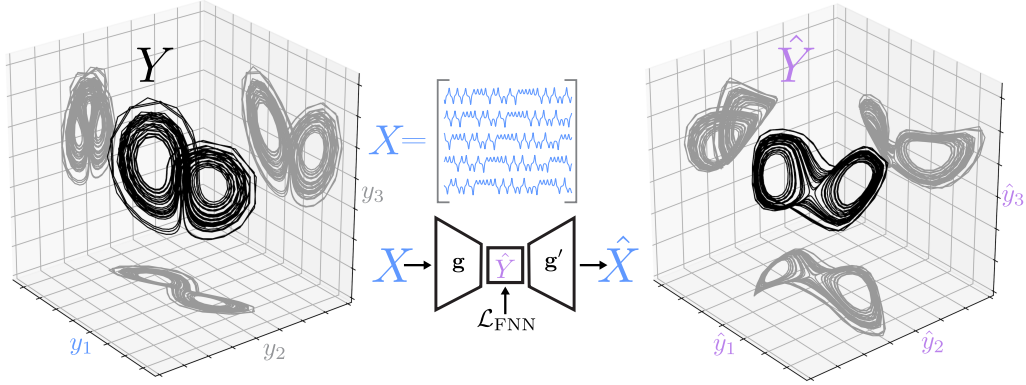


Figure 1. Overview of problem and approach. A univariate time series  $y_1(t)$  is observed from a multivariate attractor  $Y = [y_1(t) \ y_2(t) \ y_3(t)]$ . This signal is converted into a time-lagged Hankel matrix  $X$ , which is used to train an autoencoder with the false-nearest-neighbor loss  $\mathcal{L}_{\text{FNN}}$ . The latent variables reconstruct the original coordinates.

- We introduce several novel metrics for comparing an inferred attractor to a system’s original attractor, and we compare these metrics to existing methods for comparing multidimensional time series.
- We find that autoencoders with our regularizer outperform existing techniques, including eigen-time-delay coordinate embedding and time-lagged independent component analysis.
- We perform exploratory experiments applying our technique to experimental systems that have previously been hypothesized to occupy strange attractors, and discover underlying attractors in datasets from climate science, neuroscience, and electrophysiology.

## 2. Background and Definitions

Suppose that a  $d$ -dimensional dynamical system  $\dot{\mathbf{y}} = \mathbf{f}(\mathbf{y}, t)$  occupies an attractor  $A$ . The time-evolving state variable  $\mathbf{y}$  may be represented abstractly by composition with a flow operator,  $\mathbf{y}(t) = \mathcal{F} \circ \mathbf{y}(t_0)$ . At any given instant in time, a measurement  $\mathbf{x}(t)$  corresponds to composition with the operator,  $\mathcal{M}$ , such that  $\mathbf{x}(t) = \mathcal{M} \circ \mathbf{y}(t) = \mathcal{M} \circ (\mathcal{F} \circ \mathbf{y}(t_0))$ , where  $d_m \equiv \dim \mathbf{x}_t$ . We define the data matrix  $X = [\mathbf{x}_1^\top \ \mathbf{x}_2^\top \ \cdots \ \mathbf{x}_N^\top]^\top$  as a collection of  $N$  evenly-spaced measurements with timestep  $\Delta t$ . Many standard unsupervised embedding techniques for dynamical systems, such as proper orthogonal decomposition or dynamic mode decomposition, implicitly require that  $d_m$  is sufficiently large that the measurement operator’s basis spans that of the original system,  $\text{span}(\mathcal{M}) \geq \text{span}(\mathcal{F})$  (Takeishi et al., 2017; Mardt et al., 2018). This condition makes it possible to infer  $A$  with sufficient measurements.

Here, we consider the case where high-dimensional time-

resolved measurements are unavailable,  $\text{span}(\mathcal{M}) < \text{span}(\mathcal{F})$ , making it more challenging to infer the underlying dynamics. A common example is the univariate case  $d_m = 1$ , such that  $X = [x_1 \ x_2 \ \cdots \ x_N]^\top$ . A standard solution in time series analysis is to augment the dimensionality of the measurements via the method of lags, in which the  $T$  previous measurements are appended to each timestep, producing a multidimensional surrogate measurement  $\mathbf{x}_i = [x_{i-T} \ x_{i-T+1} \ \cdots \ x_i]^\top$ . In principle,  $T$  should be large enough that  $x$  (and potentially  $\mathbf{y}$ ) undergoes sufficient variation to provide information about the dynamics of each component  $y_j$  of the underlying system. After augmenting dimensionality with lags, the measurement matrix  $X \in \mathbb{R}^{T \times N}$  has Hankel structure along its diagonals, and here it will serve as the input for an unsupervised learning problem:

We seek a parametric transformation  $\hat{\mathbf{y}} = \mathbf{g}_\theta(\mathbf{x})$  such that  $\hat{Y} \sim Y$ , where  $\hat{Y}, Y \in \mathbb{R}^{N \times L}$ .  $Y = [\mathbf{y}_1^\top \ \mathbf{y}_2^\top \ \cdots \ \mathbf{y}_N^\top]^\top$  refers to the point cloud corresponding to a finite-duration sample from the true attractor  $A$ , and the point cloud  $\hat{Y} = [\hat{\mathbf{y}}_1^\top \ \hat{\mathbf{y}}_2^\top \ \cdots \ \hat{\mathbf{y}}_N^\top]^\top$  refers to the embedding coordinates generated from  $\mathbf{x}$  at the same timepoints. We seek the similarity transform  $\hat{Y} \sim Y$ , rather than  $\hat{Y} = Y$  or even  $\hat{Y} \cong Y$ , because a univariate measurement series cannot contain information about the relative symmetry, chirality, or scaling of the different coordinates comprising  $\mathbf{y}$ . This can be understood by considering the case where the measurement  $\mathcal{M}$  corresponds to a projection of the dynamics onto a single axis, a process that discards information about the relative ordering of the original coordinates.

For general dynamical systems, the embedding function  $\mathbf{g}$  satisfies several properties. While  $\dim \mathbf{g} = L$ , because the embedding coordinates may be linearly dependent, the dimension of the embedded attractor  $d_E$  satisfies  $d_E \leq L$ .

Additionally, for chaotic systems the original attractor  $A$  may be a manifold with fractal dimension  $d_F \leq d$ , which can be estimated from  $Y$  using box-counting or related algorithms. Under weak assumptions on  $\mathbf{f}$  and  $\mathcal{M}$ , the Whitney embedding theorem states that a  $d_E$ -dimensional embedding  $E$  will be diffeomorphic to  $A$ , so long as  $d_E > 2d_F$ . This condition ensures that essential properties of the attractor relevant to the dynamics of the system (and thus relevant to prediction and characterization) are retained in the embedded attractor. Thus, as long as the learned function  $\mathbf{g}$  is smooth over  $X$ , and  $d_E$  is sufficiently large, then the embedding generated from a univariate measurement will retain essential topological information about the full attractor  $A$ .

However, while the Whitney embedding theorem affirms the feasibility of reconstructing  $A$  given a low-dimensional measurement, it does not prescribe a specific method for finding  $\mathbf{g}$  from an arbitrary complex time series. In practice  $\mathbf{g}$  is commonly constructed using the method of delays, in which the embedded coordinates comprise a finite number of time-lagged coordinates,  $\mathbf{g}(\mathbf{x}_i) = [x_{i-d_E\tau} \ x_{i-(d_E-1)\tau} \ \cdots \ x_i]^\top$ . This technique is motivated by Takens' theorem, a corollary of the Whitney theorem that states that  $\hat{Y}$  will be diffeomorphic to  $Y$  for *any* choice of lag time  $\tau$  (Takens, 1981). However, the topological properties of  $\hat{Y}$  strongly vary with the choice of lag time  $\tau$ .

### 3. Related Work

The method of lagged coordinates for state space reconstruction is widely used in fields ranging from ecology, to medicine, to meteorology (Abarbanel et al., 1993; Sugihara et al., 2012; Deyle & Sugihara, 2011). Many contemporary applications of the technique still use classical methods developed by Fraser & Swinney (1986) and Kennel et al. (1992) in order to determine, respectively,  $\tau$  and  $d_E$  for Takens' theorem. Several influential generalizations of the lagged coordinates method use statistical arguments to reduce the sensitivity of the resultant embeddings to changes in hyperparameters or embedding timescale (Cao, 1997; Pecora et al., 2007). Other works have explored the use of multiple time lags (Garcia & Almeida, 2005) and the selection of time lags based on topological considerations (Tran & Hasegawa, 2019). Dhir et al. (2017) train a variational autoencoder to time-advance embedded coordinates, using a Bayesian framework to select values for  $\tau$  and  $d_E$ .

Several recent studies instead construct  $\mathbf{g}(\cdot)$  via singular-value decomposition of the Hankel matrix, producing a set of "eigen-time-delay coordinates" (Juang & Pappa, 1985; Broomhead & Jones, 1989; Giannakis & Majda, 2012). These have recently been used to construct high-dimensional linear operators that can evolve the underlying dynamics

(Brunton et al., 2017; Champion et al., 2019). Other methods of constructing  $\mathbf{g}$  include time-delayed independent components (Pérez-Hernández et al., 2013) and Laplacian eigenmaps (Erem et al., 2016; Han et al., 2018). Recent studies have sought to construct  $\mathbf{g}(\cdot)$  using feedforward neural networks (Jiang & He, 2017) and reservoir computers (Lu et al., 2018).

Below, we describe a novel embedding technique that determines  $\mathbf{g}$  using an autoencoder with a sparsity-promoting latent-space regularizer, which seeks  $d_E \approx d$ ,  $d_E \leq L$ . Several existing regularizers also encourage latent sparsity by decorrelating latent units (Cogswell et al., 2016). Recent applications of autoencoders for reconstructing dynamics from high-dimensional measurements also introduce methods for encouraging dynamical sparsity, primarily by enforcing low rank in a linear time-evolution operator acting on the latent space (Sun et al., 2019; She et al., 2018; Costa et al., 2019).

### 4. Methods

We create physically-informative attractors from time series by training an autoencoder on the Hankel measurement matrix for the system:  $\hat{X} = \mathbf{g}'(\mathbf{g}(X)) \approx X$ , with  $\mathbf{g}$  applied columnwise. After training the autoencoder, an embedding may be generated either from training data or unseen test data using the encoder portion of the network,  $\hat{Y} = \mathbf{g}(X)$ . To train  $\mathbf{g}'$  and  $\mathbf{g}$ , we introduce a new sparsity-promoting loss  $\mathcal{L}_{\text{FNN}}$ , which functions as a latent-space regularizer, and we find similar results across multiple autoencoder architectures (described below). Our approach is outlined in Figure 1.

Our loss function  $\mathcal{L}_{\text{FNN}}$  represents a variational formulation of the false-nearest-neighbors method, a popular heuristic for determining the appropriate embedding dimension  $d_E$  when using the method of lags (Kennel et al., 1992). The intuition behind the technique is that a  $d$ -dimensional embedding with too few dimensions will have many overlapping points, which will undergo large separation when the embedding is lifted to  $d + 1$ . These points correspond to false neighbors, which only co-localize in  $d$  dimensions due to having overlapping projections (Figure 2). The traditional false-nearest-neighbors technique asserts that the true embedding dimension  $d_E$  occurs when the fraction of false nearest neighbors first approaches zero as  $d$  increases. Here, we implement the method as a regularizer acting on each batch of latent activations during training.

Let  $h \in \mathbb{R}^{B \times L}$  denote activations of a latent layer with  $L$  units, generated when the network is given an input batch of size  $B$ . For the embedding problem studied here,  $h$  corresponds to a partial embedding  $\sim \hat{Y}$  generated from an input comprising  $B$  length- $T$  rows randomly sampled from the full Hankel measurement matrix  $X$ . However, here we

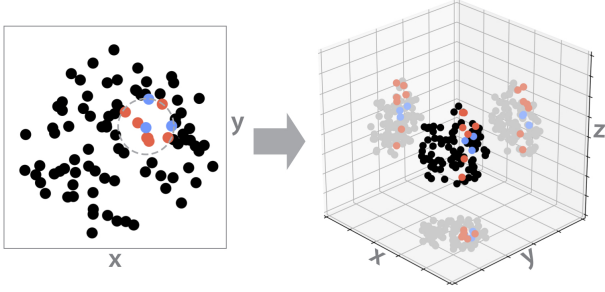


Figure 2. A set of near neighbors in a two-dimensional projection of three-dimensional point cloud (circled blue and red points). False neighbors (red) separate when the system is lifted to a higher dimension.

use general notation to emphasize that this regularizer can be applied to hidden layers in an arbitrary network.

We define the dimension-indexed, pairwise Euclidean distance  $D \in \mathbb{R}^{B \times B \times L}$  among all points in the batch,

$$D_{abm}^2 = \sum_{i=1}^m (h_{ai} - h_{bi})^2.$$

This tensor describes the Euclidean distance between samples  $a$  and  $b$  when only the first  $m$  latent dimensions are considered. Calculation of this quantity therefore breaks ordering invariance among the latent dimensions.

Column-wise sorting of  $D_{abm}$  may be used to define the index tensor  $g \in \mathbb{R}^{B \times B \times T}$ , where each column  $g_{a:,m}$  contains the indices of all members of the batch sorted in ascending order of their relative distance from  $a$  when only the first  $m$  dimensions are considered. We use  $g$  to define the sorted distance tensor and the shifted sorted distance tensor,

$$\tilde{D}_{abm} = \sum_{b=1}^B \delta_{b,g_{abm}} D_{abm}, \quad \tilde{D}'_{akm} = \sum_{b=1}^B \delta_{b,g_{ab,m-1}} D_{abm},$$

where  $\tilde{D}_{abm} \in \mathbb{R}^{B \times B \times L}$  corresponds to  $D_{abm}$  sorted columnwise, while  $\tilde{D}'_{abm} \in \mathbb{R}^{B \times B \times (L-1)}$  corresponds to sorting each column of  $D_{abm}$  according to the sort order of the previous column. These quantities allow computation of the normalized change in distance to a given neighbor as  $m$  increases, labelled by its relative distance,  $S_{abm} = (D_{abm}^2 - \tilde{D}_{abm}^2) / \tilde{D}_{abm}^2$ , where  $m \geq 2$ .

A false neighbor is defined as an  $m-1$  dimensional near-neighbor that undergoes a jump greater than  $R_{\text{tol}}$  when lifted to  $m$  dimensions,

$$R_{abm} = \begin{cases} 1 & S_{abm} \geq R_{\text{tol}} \\ 0 & S_{abm} < R_{\text{tol}} \end{cases}.$$

The threshold  $R_{\text{tol}}$  can be chosen arbitrarily; in practice we find that it has little effect on our results, and so we set it to a constant value  $R_{\text{tol}} = 10$  (a standard value) for all experiments (Kennel et al., 1992).

In regions of the attractor where the dynamics proceeds relatively quickly, the uniformly-spaced time series comprising  $\hat{Y}$  undersamples the attractor. This can lead to points undergoing large shifts in position relative to the scale of the attractor as  $m$  increases, leading to an additional criterion for whether a given point is considered a false neighbor. We define the characteristic size of the attractor in the first  $m$  latent coordinates,

$$\mathcal{R}_m^2 = \frac{1}{mB} \sum_{b=1}^B \sum_{i=1}^m (h_{bi} - \bar{h}_i)^2,$$

where  $\bar{h}_i = (1/B) \sum_{b=1}^B h_{bi}$ . This quantity defines a second criterion,

$$A_{akm} = \begin{cases} 1 & \tilde{D}_{akm} \geq A_{\text{tol}} \mathcal{R}_m \\ 0 & \tilde{D}_{akm} < A_{\text{tol}} \mathcal{R}_m \end{cases}.$$

The behavior of the regularizer does not strongly vary with  $A_{\text{tol}}$ , as long as this hyperparameter is set to a sufficiently large value. We therefore set  $A_{\text{tol}} = 2.0$ , a standard value in the literature, and keep it constant for all experiments.

We define the elementwise false neighbor matrix as satisfying either or both these criteria,

$$F_{abm} = \Theta(R_{abm} + A_{abm})$$

where  $\Theta$  denotes the left-continuous Heaviside step function,  $\Theta(x) = 1, x > 0$ ,  $\Theta(x) = 0, x \leq 0$ . We next contract dimensionality by averaging this quantity  $F_{abm}$  across both the batch and the set of  $K$  nearest neighbors to  $a$ ,

$$\bar{F}_m = \frac{1}{KB} \sum_{k=1}^K \sum_{b=1}^B F_{abm}.$$

The hyperparameter  $K$  determines how many neighbors are considered ‘‘close’’ enough to be informative about the topology of the attractor. Because varying this hyperparameter has a similar effect to changing  $B$ , we set  $k = \lceil 0.01B \rceil$  and otherwise leave this parameter constant. Having obtained the dimension-wise fractional false neighbor count  $\bar{F}_m$ , we now calculate the false neighbor loss,

$$\mathcal{L}_{\text{FNN}}(h) = \sum_{m=2}^L (1 - \bar{F}_m(h)) \bar{h}_m^2. \quad (1)$$

The loss thus has the form of an activity regularization acting on the latent coordinates. Taken together, the overall loss function for the autoencoder has the form

$$\mathcal{L}(X, \hat{X}, \hat{Y}) = \|X - \hat{X}\|^2 + \lambda \mathcal{L}_{\text{FNN}}(\hat{Y})$$



where  $\|\cdot\|^2$  denotes the mean square error averaged across the batch, and  $\lambda$  is a hyperparameter controlling the relative strength of the regularizer.

## 5. Experiments

**Models.** In order to illustrate the robustness of the loss function across different architectures, we use two standard autoencoder models for all experiments: a single-layer long short-term memory network (LSTM) and a three-layer multilayer perceptron (MLP), each with  $L = 10$  latent units. These architectures were chosen because they have approximately equal numbers of parameters (520 and 450, respectively), which is small compared to the minimum of 5000 training examples used for all datasets (see supplementary material for additional model details). We obtain comparable results with both models, and we include the MLP results in the appendices.

Across all experiments, the only hyperparameters that are tuned are the regularizer strength  $\lambda$  and the learning rate  $\gamma$ . Because embedding of an unknown experimental dataset is, in general, an unsupervised learning problem, we do not change the network architecture, optimizer, and other parameters. As a general heuristic, we tune  $\lambda$  to be just small enough to avoid dimensionality collapse in the reconstructed attractor (an easily-recognized phenomenon discussed in the next section), and we adjust  $\gamma$  only to ensure convergence within the constant number of training epochs used in all experiments. For all results, we perform 5 replicates with random initialization.

**Datasets.** We study datasets corresponding to several chaotic or quasiperiodic systems: the three-dimensional Lorenz “butterfly” attractor, the three-dimensional Rössler attractor, a ten-dimensional Lotka-Volterra ecosystem, a three-dimensional quasiperiodic torus, and an experimental dataset corresponding to centroid measurements of a chaotic double pendulum (an effectively four-dimensional system over short timescales) (Asseman et al., 2018). Due to space constraints, we include the Rössler and torus results in the appendices; however these results are consistent with those observed on other datasets. For all datasets, 5000 timepoints are used to construct separate Hankel matrices for training and validation of  $\mathbf{g}$  and  $\mathbf{g}'$ , and 5000 separate timepoints are used as a test dataset for embedding. For exploratory analysis of datasets with unknown governing equations, we use datasets corresponding to: temperature measurements of the irregularly-firing “Old Faithful” geyser; a human electrocardiogram; hourly electricity usage measurements for 321 households; and spiking rates for neurons in a mouse thalamus. Dataset timescales and sampling rates are chosen so that the dominant Fourier peaks align.

**Baselines.** As baselines, we use the eigen-time-delay coor-

dinates method (ETD) (Broomhead & Jones, 1989; Brunton et al., 2017), time-lagged independent component analysis (tICA) (Pérez-Hernández et al., 2013), and replicates of the autoencoders with  $\lambda = 0$ .

**Evaluation.** Because time series embedding constitutes an unsupervised learning problem, for testing performance against baselines, we train our models by choosing a single coordinate  $y_1(t)$  from a known dynamical system  $\mathbf{y}(t)$ , which we use to construct a Hankel measurement matrix  $X_{\text{train}}$ . We then train our autoencoder on  $X_{\text{train}}$ , and then use it to embed the Hankel matrix of unseen data  $X_{\text{test}}$  from the same system, producing the reconstruction  $\hat{Y}_{\text{test}}$ . We then compare  $\hat{Y}_{\text{test}}$  to  $Y_{\text{test}}$ , a sample of the full attractor at the same timepoints. Because the number of latent coordinates  $L$  is the same for all models, when comparing point clouds between the full attractor with dimension  $d$  and the reconstructed attractor with dimension  $L$ , we consider only the first  $d$  dimensions of  $\hat{Y}$ ; except for the dimension similarity metric described below, where we instead pad  $Y$  with  $(L - d)$  zeros columnwise.

**Evaluation metrics.** We introduce several methods for comparing the original system  $Y$  with its reconstruction  $\hat{Y}$ . We emphasize that this comparison does not occur during training (the autoencoder only sees one coordinate); rather, we use these metrics to assess how well our unsupervised models can reconstruct known systems. We describe these metrics in greater detail in the supplementary materials.

*Pointwise comparison.* We first evaluate the degree to which each point  $\hat{\mathbf{y}}_i$  differs from its true location  $\mathbf{y}_i$ . Because  $X$  does not contain information about the symmetry group or chirality of the full attractor, when computing pointwise similarity between the true and embedded attractors, we first align the two datasets using the Procrustes transform,  $P = \arg \min_{\tilde{P}} \|\tilde{P}\hat{Y} - Y\|$  such that  $\tilde{P}^\top \tilde{P} = I$ . This transformation registers  $\hat{Y}$  to  $Y$  via translation, rotation, reflection, but *not* shear. For example, after this transformation, mirror images of a spiral would become congruent, whereas a sphere and ellipsoid would not. After computing  $P$ , we may compare  $P\hat{Y}$  to  $Y$  via a variety of standard metrics, including the Euclidean distance and the dynamic time warping distance. We normalize these values across datasets by dividing by the summed featurewise variance and convert to similarities by subtracting from one. The resulting similarities are comparable to the pointwise attractor similarity originally proposed by Diks et al. (1996).

*Neighbor fidelity.* We evaluate the degree to which an embedded point  $\hat{\mathbf{y}}_i$  retains information about its true  $k$ -nearest-neighbors on the original attractor. The *simplex distance* (Sugihara & May, 1990) measures the average distance between a point  $\hat{\mathbf{y}}_i$  and its predicted position at a point  $\tau$  timesteps in the future, based on the centroid of the set  $\Omega$  comprising its  $k$ -nearest-neighbors,  $\tilde{\mathbf{y}}_i = (1/k) \sum_{j \in \Omega} \hat{\mathbf{y}}_j$ .

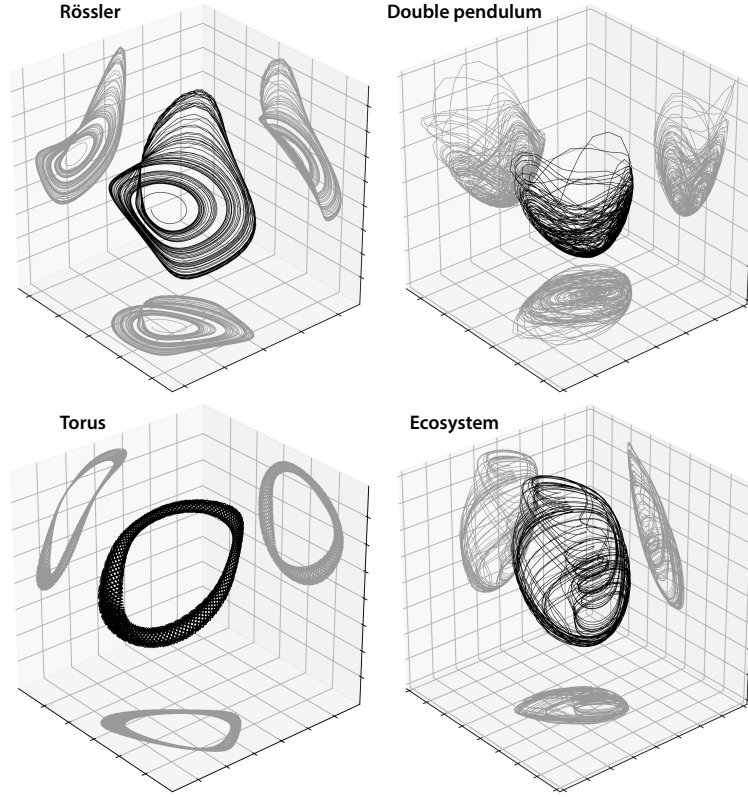


Figure 3. Embeddings produced by the autoencoder with  $\mathcal{L}_{\text{FNN}}$ , trained on only the first coordinate of each system.

We define the accumulated difference  $C$  between the predicted location  $\hat{\mathbf{y}}_i$  and the observed location  $\hat{\mathbf{y}}_{i+\tau}$  at a time  $\tau$ ,

$$C(\hat{Y}, \tau) = \frac{1}{N - \tau} \sum_{i=1}^N \sum_{m=1}^L (\hat{Y}_{i+\tau, m} - \tilde{Y}_{i, m})^2 / \sum_{m=1}^L \text{Var}(Y)$$

where  $\text{Var}(Y) \in \mathbb{R}^L$  denotes the dimension-wise variance. Here we hold fixed  $k = d, \tau = 2T$ , because, consistent with previous studies, changing these parameters does not significantly affect any reported comparisons. We calculate  $C(\hat{Y}, \tau)$  and  $C(Y, \tau)$ , and define the *Simplex Similarity*,  $\mathcal{S}_{\text{simp}}(\hat{Y}, Y, \tau) = 1 - |C(Y, \tau) - C(\hat{Y}, \tau)| / |1 - C(Y, \tau)|$ .

We also define a new, parameter-free *Neighbor Similarity*  $\mathcal{S}_{\text{nn}}$  proportional to the number  $\kappa_i(k)$  of the  $k$  closest neighbors to  $\hat{\mathbf{y}}_i$  that also fall within the  $k$  closest neighbors to  $\mathbf{y}_i$ . It is always the case that  $\kappa_i(N) = N \forall i$ , and for a perfect reconstruction,  $\kappa_i(k) = k \forall i$ . We define the coverage similarity,  $\mathcal{S}_{\text{nn}}$  similarly to the AUC-ROC, by first averaging  $\bar{\kappa}(k) = \sum_{i=1}^N \kappa_i(k)$ , and then sweeping  $k$  and calculating the total area between the observed  $\bar{\kappa}(k)$  and the perfect case  $\bar{\kappa}(k) = k$ . We normalize this value by the expected  $\bar{\kappa}(k)$  for a random sort (given analytically by the hypergeo-

metric distribution as  $\bar{\kappa}(k) = k^2/N$ ), and we subtract this quantity from one to produce a similarity metric,

$$\mathcal{S}_{\text{nn}} = \sum_k \frac{\bar{\kappa}(k) - k^2/N}{k - k^2/N}.$$

*Global properties.* We also introduce several measures that determine how well the embedded attractor  $\hat{Y}$  captures the physical properties of the full attractor  $Y$ . A basic, informative property of a dynamical system  $\dot{\mathbf{y}}(t)$  is its dimensionality,  $d = \dim(\mathbf{y})$ , the minimum number of distinct variables necessary to fully specify the dynamics. For a given embedding  $\hat{Y}$ , we define the embedding dimension  $d_E$  in terms of the relative activity of each latent neuron  $\text{Var}(\hat{\mathbf{y}})$ . The *Dimension Similarity*,  $\mathcal{S}_{\text{dim}}$  represents the dimension-wise difference between the activities of each latent dimension of  $\hat{\mathbf{y}}$  and of each true coordinate  $\mathbf{y}$ . We normalize by the total variance, and subtract from one,  $\mathcal{S}_{\text{dim}} = 1 - \|\text{SORT}(\text{Var}(\mathbf{y})) - \text{SORT}(\text{Var}(\hat{\mathbf{y}}))\| / \|\text{Var}(\mathbf{y})\|$ , where sorting is applied dimensionwise.

We define the *Topological Similarity*  $\mathcal{S}_{\text{homol}}$  to measure the degree to which  $\hat{Y}$  retains essential structural features of  $Y$ , such as the presence of holes, voids, and extrema (such as the “double scrolls” of the Lorenz attractor). We cal-

culate this metric using the bottleneck distance, a distance between two point clouds weighted by the persistence of different topological features as the cloud is coarse-grained across increasing length scales (for more details about persistent homology, see Edelsbrunner & Harer (2008)). This technique was recently found to effectively capture global similarity between strange attractors (Venkataraman et al., 2016; Tran & Hasegawa, 2019). Following previous work, we normalize the bottleneck distance by the distance between the original attractor  $Y$  and a null attractor with no salient features, and subtract from one to generate a similarity,  $\mathcal{S}_{\text{homol}}$ .

Lastly, we define the *Fractal Similarity*  $\mathcal{S}_{\text{corr}}$  corresponding to one minus the symmetric absolute percent difference between the correlation fractal dimension of  $\hat{Y}$  and of  $Y$ . We use the correlation dimension instead of related physical properties (such as the Lyapunov exponent, or Kolmogorov-Sinai entropy) because, unlike other properties, the correlation dimension can be robustly measured in a parameter-free manner, without random subsampling of points, using a popular algorithm by Grassberger & Procaccia (1983).

## 6. Results

### 6.1. Evaluation with known attractors

Figure 3 shows example embeddings of datasets with known attractors using the LSTM autoencoder with  $\mathcal{L}_{\text{FNN}}$ , illustrating the qualitative similarity of the learned embeddings to the true attractors. The corresponding embedding of the Lorenz attractor was previously shown in Figure 1. Table 1 summarizes quantitative evaluation of reconstruction accuracy for the Lorenz model, double pendulum experiment, and ecosystem model datasets. We obtain similar results for the torus and Rössler datasets, as well as for all datasets with the alternative MLP model; we include these additional results in the appendix. The table shows that the regularized network either matches or improves the quality of the embedding across a variety of different metrics, although the performance varies by metric and dataset.  $\mathcal{S}_{\text{dim}}$  consistently improves with the regularizer, demonstrating that  $\mathcal{L}_{\text{FNN}}$  fulfills its primary purpose of generating a latent space with appropriate effective dimensionality  $d_E$ . Importantly, this effect is not simply due to  $\mathcal{L}_{\text{FNN}}$  indiscriminately decreasing the effective latent space; for the ecosystem dataset,  $d = L = 10$  and so achieving high  $\mathcal{S}_{\text{dim}}$  requires that all latent units remain active after training.

$\mathcal{S}_{\text{nn}}$  and  $\mathcal{S}_{\text{proc}}$  both indicate that the regularized LSTM consistently captures global neighborhood properties and relative placement of points compared to the full-dimensional attractor  $Y$ . Performance is weaker for  $\mathcal{S}_{\text{simp}}$  and  $\mathcal{S}_{\text{corr}}$ , which we hypothesize arises due to information loss from the constraints on the latent space. We observe that worse perfor-

Table 1. Results for the Lorenz, experimental pendulum, and model ecosystem datasets. Errors correspond to standard deviations over 5 replicates with random weights. For each row, the maximum value, as well as any other values with overlapping error ranges, is marked in bold.

METRIC	TICA	ETD	LSTM	LSTM-FNN
LORENZ				
$\mathcal{S}_{\text{SIMP}}$	0.153	0.235	<b><math>0.63 \pm 0.09</math></b>	<b><math>0.68 \pm 0.07</math></b>
$\mathcal{S}_{\text{CORR}}$	<b>0.985</b>	<b>0.978</b>	$0.87 \pm 0.02$	<b><math>0.98 \pm 0.02</math></b>
$\mathcal{S}_{\text{HOMOL}}$	0.123	<b>0.668</b>	$0.04 \pm 0.03$	$0.3 \pm 0.1$
$\mathcal{S}_{\text{PROC}}$	0.037	0.212	$0.20 \pm 0.03$	<b><math>0.37 \pm 0.02</math></b>
$\mathcal{S}_{\text{DTW}}$	0.21	0.27	$0.31 \pm 0.03$	<b><math>0.47 \pm 0.03</math></b>
$\mathcal{S}_{\text{NN}}$	0.296	<b>0.384</b>	$0.25 \pm 0.06$	<b><math>0.4 \pm 0.02</math></b>
$\mathcal{S}_{\text{DIM}}$	0.394	0.628	$-0.06 \pm 0.08$	<b><math>0.66 \pm 0.01</math></b>
DOUBLE PENDULUM				
$\mathcal{S}_{\text{SIMP}}$	0.856	0.51	$0.74 \pm 0.04$	<b><math>0.98 \pm 0.07</math></b>
$\mathcal{S}_{\text{CORR}}$	0.861	0.822	<b><math>0.966 \pm 0.006</math></b>	<b><math>0.986 \pm 0.008</math></b>
$\mathcal{S}_{\text{HOMOL}}$	0.202	0.176	$0.19 \pm 0.02$	<b><math>0.25 \pm 0.02</math></b>
$\mathcal{S}_{\text{PROC}}$	0.001	0.003	$0.008 \pm 0.005$	<b><math>0.016 \pm 0.006</math></b>
$\mathcal{S}_{\text{DTW}}$	0.069	<b>0.108</b>	$0.11 \pm 0.01$	<b><math>0.132 \pm 0.008</math></b>
$\mathcal{S}_{\text{NN}}$	0.031	0.055	$0.042 \pm 0.002$	<b><math>0.060 \pm 0.001</math></b>
$\mathcal{S}_{\text{DIM}}$	-1.914	0.927	$-0.8 \pm 0.3$	<b><math>0.97 \pm 0.01</math></b>
ECOSYSTEM				
$\mathcal{S}_{\text{SIMP}}$	0.628	0.619	<b><math>0.85 \pm 0.008</math></b>	<b><math>0.87 \pm 0.02</math></b>
$\mathcal{S}_{\text{CORR}}$	<b>0.890</b>	0.820	$0.877 \pm 0.004$	<b><math>0.888 \pm 0.003</math></b>
$\mathcal{S}_{\text{HOMOL}}$	0.066	0.256	$0.09 \pm 0.04$	<b><math>0.33 \pm 0.03</math></b>
$\mathcal{S}_{\text{PROC}}$	0.024	0.025	$-0.1 \pm 0.05$	<b><math>0.08 \pm 0.05</math></b>
$\mathcal{S}_{\text{DTW}}$	0.115	0.051	$0.05 \pm 0.03$	<b><math>0.15 \pm 0.03</math></b>
$\mathcal{S}_{\text{NN}}$	0.133	0.146	$0.304 \pm 0.004$	<b><math>0.313 \pm 0.005</math></b>
$\mathcal{S}_{\text{DIM}}$	0.60	0.664	$0.51 \pm 0.05$	<b><math>0.92 \pm 0.02</math></b>

mance is generally obtained for metrics that are close to one on the baselines; the primary improvements offered by  $\mathcal{L}_{\text{FNN}}$  seem to arise from capturing properties for which the baseline models strongly underperform.

Importantly, we observe that the regularized autoencoder nearly always improves on the non-regularized model, suggesting that the regularizer has a clear and beneficial effect on the representations obtained by the model. We hypothesize that the stronger test performance of the regularized vs. non-regularized model occurs because the regularizer reduces overfitting by compressing the model (reducing latent dimensionality), thereby avoiding overfitting. This effect may explain why models with the regularizer generally exhibit lower variance, due to a constraints on the latent space reducing the range of available representations.

We emphasize the consistency of our results across these datasets, which span from low-dimensional chaos (Lorenz and Rössler attractors), high-dimensional chaos (the ecosystem model), noisy and non-stationarity experimental data (the double pendulum experiment), and non-chaotic regular

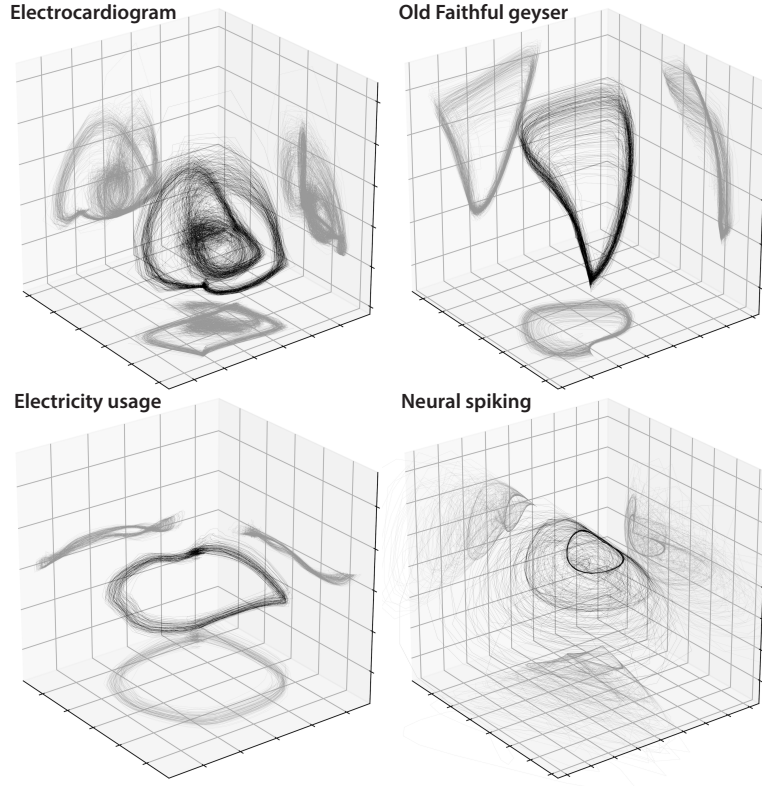


Figure 4. Embeddings of an electrocardiogram (160 heartbeats), temperature measurements of the erupting “Old Faithful” geyser in Yellowstone National Park (200 eruptions), average electricity usage by 321 households (200 days), and spiking activity of a single neuron in a mouse thalamus. Datasets are sampled to have matching characteristic timescales, and then partitioned into 10000 timepoints each for fitting and embedding.

dynamics (the torus).

## 6.2. Empirical properties of the FNN loss function

We next investigate in detail the effect of the regularizer strength  $\lambda$  on embedding. Figure S1A shows the effect of increasing the regularizer strength on the variance of the activity of the  $L = 10$  ranked latent coordinates for embeddings of the Lorenz dataset. Identical experiments with the MLP model are included in the appendix. As  $\lambda$  increases, the distribution of activation across latent variables develops increasing right skewness, eventually producing a distribution of activations similar to that of weighted principal components. Figure S1B shows the final dimensionality error  $1 - \mathcal{S}_{\text{dim}}$  for the network as a function of the regularizer strength. The plots show that the dimensionality accuracy of the learned representation improves as long as  $\lambda$  is greater than a threshold value. However, the error begins to increase if  $\lambda$  becomes too large, due to the learned attractor becoming overly flattened, and thus further from the correct dimensionality. This nonlinearity implies a simple heuristic for setting  $\lambda$  for an unknown dataset: keep increasing lambda

until the effective dimensionality of the latent space rapidly decreases, and then vary it no further.

## 6.3. Application to datasets with unknown attractors

To demonstrate the potential utility of our approach for exploratory analysis of unknown time series, we next embed several time series datasets for which the governing equations are unknown, but for which low-dimensional attractors have previously been hypothesized. Figure 4 shows embeddings of various systems using the FNN loss with the LSTM model. For all systems, a different training dataset is used to construct  $g(\cdot)$  than the testing dataset plotted. Several qualitative features of the embedded attractors are informative. For the electrocardiogram dataset, the model successfully creates a “nested loop” geometry reminiscent of that described in analytical models of the heart (Kaplan & Cohen, 1990). This structure arises despite the plotted embedding corresponding to an ECG from a different patient than the one used to train the model. For the Old Faithful dataset, the model identifies a low-dimensional quasi-periodic attractor that is consistent with a long-suspected hypothesis that the



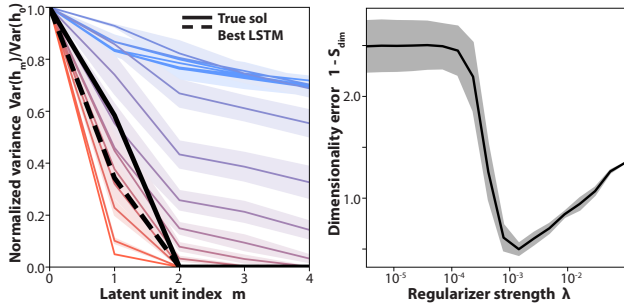


Figure 5. (A) The distribution of normalized latent variances as a function of regularizer strength from  $\lambda = 0$  (blue) to  $\lambda = 0.1$  (red), with the normalized variance for the full solution (solid black line) and for the final best-performing LSTM (dashed black line). (B) The dimensionality error  $1 - \mathcal{S}_{\text{dim}}$  as a function of  $\lambda$ . Error ranges correspond to 5 replicates.

geyser’s nearly-regular dynamics arise from a strange attractor (arising from a small number of governing pressure and temperature state variables) (Nicholl et al., 1994). The dense regions of the attractor correspond to eruption events—which occur with consistent, stereotyped dynamics—while the diffuse, fan-like region of the attractor corresponds to the slow recovery period between firings, which has a broader range of dynamics and timings. For the electricity usage dataset, which has previously been used as a benchmark for time series forecasting (Rangapuram et al., 2018), the embedding reveals a circular limit cycle consistent with a stable daily usage cycle. For the mouse neuron spiking rate dataset, the model identifies a double-limit-cycle structure, consistent with observations from higher-dimensional measurements that suggest that the neuronal dynamics occupy a low-dimensional intrinsic attractor manifold (Chaudhuri et al., 2019).

## 7. Conclusion

We have introduced a method for reconstructing the attractor of a dynamical system, even when only a low-dimensional time series measurement of the system is available. By comparing our technique to existing methods across a variety of complex time series, we have shown that our approach constructs informative, topologically-accurate embeddings that closely match the dimensionality of the original time series. Because our technique essentially has one governing hyperparameter, the regularizer strength  $\lambda$ , it may easily be applied to unknown time series, which we have demonstrated using a variety of datasets from areas spanning from electrophysiology to neuroscience. Generalizing our technique to multidimensional time series is relatively straightforward, and we hope that this embedding technique can, in future work, form a basis for learning empirical time

evolution operators for the dynamics. We hope that our publicly-available code will facilitate research in this direction.

## 8. Acknowledgements

We thank Chris Rycroft, Brian Matejek, and Daniel Forger for their comments on the project and manuscript. W. G. was supported by the NSF-Simons Center for Mathematical and Statistical Analysis of Biology at Harvard University, NSF Grant No. DMS-1764269, and the Harvard FAS Quantitative Biology Initiative.

## 9. Code availability

Code for this study is available at:

<https://github.com/williamgilpin/fnn>

## Supplementary material

### A. Description of reference datasets

**Lorenz attractor.** The Lorenz equations are given by

$$\begin{aligned}\dot{x} &= \sigma(y - x) \\ \dot{y} &= x(\rho - z) - y \\ \dot{z} &= xy - \beta z\end{aligned}$$

We use parameter values  $\sigma = 10$ ,  $\rho = 28$ ,  $\beta = 2.667$ . The system was simulated for 500 timesteps, with a stepsize  $\Delta t = 0.004$ . The system was then downsampled by a factor of 10. We fit the model using  $x(t)$ , which we divide into separate train, validation, and test datasets corresponding to the first, second, and last 5000 timepoints from a 125000 step trajectory.

**Rössler attractor.** The Rössler attractor is given by

$$\begin{aligned}\dot{x} &= -y - z \\ \dot{y} &= x + ay \\ \dot{z} &= b + z(x - c)\end{aligned}$$

We use parameter values  $a = 0.2$ ,  $b = 0.2$ ,  $c = 5.7$ , which produces a chaotic attractor with the shape of a Möbius strip. The system was simulated for 2500 timesteps, with a stepsize  $\Delta t = 0.125$ . The system was then downsampled by a factor of 10. We fit the model using  $x(t)$ , which we divide into separate train, validation, and test datasets corresponding to the first, second, and last 5000 timepoints.

**Ecological resource competition model.** We use a standard resource competition model, a variant of the Lotka-Volterra model that is commonly used to describe scenarios in which  $n$  distinct species compete for a pool of  $k$  distinct nutrients. We let  $N_i(t)$  denote the abundance of species  $i$ , and  $R_j(t)$  denote the availability of resource  $j$ .

$$\begin{aligned}\dot{N}_i &= N_i \left( \mu_i(R_1, \dots, R_k) - m_i \right) \\ \dot{R}_j &= D(S_j - R_j) - \sum_{i=1}^n c_{ji} \mu_i(R_1, \dots, R_k) N_i\end{aligned}$$

where the species-specific growth rate is given by

$$\mu_i(R_1, \dots, R_k) = \min \left( \frac{r_i R_1}{K_{1i} + R_1}, \dots, \frac{r_i R_k}{K_{ki} + R_k} \right).$$

This model is strongly chaotic for a range of parameter values, and it was recently used to argue that chaotic dynamics may account for the surprising stability in long-term population abundances of competing phytoplankton species in the ocean (Huisman & Weissing, 1999). We use parameter values from this study, which corresponds to  $n = 5$  species and

$k = 5$  resources. The full parameter values are:  $D = 0.25$ ,  $r_i = r = 1$ ,  $m_i = m = 0.25$ ,  $\mathbf{S} = [6, 10, 14, 4, 9]$ ,

$$\mathbf{K} = \begin{bmatrix} 0.39 & 0.34 & 0.3 & 0.24 & 0.23 \\ 0.22 & 0.39 & 0.34 & 0.3 & 0.27 \\ 0.27 & 0.22 & 0.39 & 0.34 & 0.3 \\ 0.3 & 0.24 & 0.22 & 0.39 & 0.34 \\ 0.34 & 0.3 & 0.22 & 0.2 & 0.39 \end{bmatrix},$$

$$\mathbf{c} = \begin{bmatrix} 0.04 & 0.04 & 0.07 & 0.04 & 0.04 \\ 0.08 & 0.08 & 0.08 & 0.1 & 0.08 \\ 0.1 & 0.1 & 0.1 & 0.1 & 0.14 \\ 0.05 & 0.03 & 0.03 & 0.03 & 0.03 \\ 0.07 & 0.09 & 0.07 & 0.07 & 0.07 \end{bmatrix}.$$

We simulate this system for 200000 units of time, with timestep  $\Delta t = 0.1$ . We discard the first 100000 timepoints to eliminate any transients, and then downsample the time series by a factor of 10. We fit the model using  $R_1(t)$ , which we divide into separate train, validation, and test datasets corresponding to the first, second, and last 5000 timepoints.

**Three-dimensional torus.** We parametrize a torus as a continuous-time, quasiperiodic dynamical system

$$\begin{aligned}\dot{x} &= -an \sin(nt) \cos(t) - (r + a \cos(nt)) \sin(t) \\ \dot{y} &= -an \sin(nt) \sin(t) + (r + a \cos(nt)) \cos(t) \\ \dot{z} &= an \cos(nt)\end{aligned}$$

where we use the parameters  $r = 1$  (the outer radius),  $a = 1/2$  (the cross-sectional radius),  $n = 15.3$  (the winding number). Because  $n$  is not an integer, trajectories of this system are non-recurring and quasiperiodic. The system was simulated for 2000 timesteps, with a stepsize  $\Delta t = 0.02$ . The time series was then downsampled by a factor of 8. We fit the model using  $x(t)$ , which we divide into separate train, validation, and test datasets corresponding to the first, second, and last 5000 timepoints.

**Double pendulum experimental dataset.** We use an existing experimental dataset comprising a 400 fps video of a double pendulum experiment, recorded on a high-speed Phantom Miro EX2 camera (Asseman et al., 2018). The video is segmented, and the centroid positions are recorded for the pivot attachment to the wall, the joint between the first and second pendula, and the tip of the second pendulum. The positions are then converted using standard trigonometry into two time series, corresponding to the angles that the first and second pendulum make with the vertical direction,  $(\theta_1, \theta_2)$ . These time series are then numerically differentiated, in order to produce a time series of the angular velocities  $(\dot{\theta}_1, \dot{\theta}_2)$ . For an ideal double pendulum, the four coordinates  $(\dot{\theta}_1, \dot{\theta}_2, \theta_1, \theta_2)$  canonically parametrize the Hamiltonian of the system, and so these four coordinates are used as the definition of the attractor. However, for the experimental dataset, the time-averaged kinetic energy  $T \propto \dot{\theta}_1^2 + \dot{\theta}_2^2$  gradually decreases throughout the course

of the experiment. This additional coordinate was not included in the reference description of the attractor, due to its slow dynamics and non-stationarity, and so it constitutes an external, non-autonomous source of variation for which the model must account.

We downsample the native resolution of these experiments by a factor of 3 and use  $\hat{\theta}_1(t)$  as the input to the model. For training and validation, we use the first and second sequences of 5000 timepoints from the first experimental dataset. For testing, we use the first 5000 timepoints from the second experimental dataset.

## B. Description of exploratory datasets

**Electrocardiogram.** We use recordings from the PhysioNet QT database, which comprises fifteen-minute, two-lead ECG recordings from multiple individuals (Laguna et al., 1997; Goldberger et al., 2000). Measurements are spaced 0.004 seconds apart. To remove high-frequency components, datasets were smoothed with a third-order Savitzky-Golay filter with a window size of 15 timepoints. The datasets are then downsampled by a factor of 10. For the analysis presented here, we use 10000 datapoints (post-subsampling) from the dataset `sel102.dat` as training data, and for testing data we use 10000 datapoints from the dataset `sel103.dat` (which corresponds to a different patient).

**Electricity usage.** We use a dataset from the UCI machine learning database (Rangapuram et al., 2018; Dua & Graff, 2017), comprising residential power consumption by 321 Portuguese households between 2012 and 2014. Raw data is measured in units of kilowatts times the fifteen minute sampling increment. We create a consolidated dataset by taking the mean of all residences at each timepoint, adjusting the sample size as necessary at each timepoint to account for missing values for some households. We use the first, second, and last 10000 timepoints training, validation, and testing data.

**Geyser temperature measurements.** We use temperature recordings from the GeyserTimes database (<https://geysertimes.org/>), which consist of temperature readings from the main runoff pool of the Old Faithful geyser, located in Yellowstone National Park. Temperature measurements start on April 13, 2015 and occur in one-minute increments. The dataset was detrended by subtracting out a version of the data smoothed with a moving average over a one-day window, which effectively removes gradual effects like seasonal variation from the attractor. For the analysis presented in the main text, we use the first, second, and last 10000 datapoints from the Old Faithful dataset as training, validation, and test datasets, respectively, corresponding to  $\approx 400$  eruptions of the geyser.

**Neural spiking.** We use a dataset from a recent study characterizing the intrinsic attractor manifold of neuronal firings of freely-moving mice (Chaudhuri et al., 2019). The raw spike count data is available from the CRCNS database (<http://crcns.org/data-sets/thalamus/th-1>), and we process this data using the authors’ included code and instructions, in order to generate time series corresponding to spiking rates for single neurons. We use the first, second, and last 10000 timepoints training, validation, and testing data.

## C. Models

We apply eigen-time-delay (ETD) embedding as described by Brunton et al. (2017), using principal components analysis as implemented in `scikit-learn` (Pedregosa et al., 2011). We apply time-structure independent component analysis (tICA) as implemented in the `MSMBuilder` software suite (Harrigan et al., 2017). For numerical integration of chaotic systems, we use built-in integrators from `scipy` (Virtanen et al., 2020).

Autoencoders are implemented using TensorFlow (Abadi et al., 2016). The single-layer LSTM autoencoder has architecture: [Input-GN-LSTM(10)-BN]-[GN-LSTM(10)-BN-ELU-Output]. The three-layer multilayer perceptron has architecture: [Input-GN-FC(10)-BN-ELU-FC(10)-BN-ELU-FC(10)-BN]-[GN-FC(10)-BN-ELU-FC(10)-BN-ELU-FC(10)-BN-ELU-Output]. ELU denotes an exponential linear unit with default scale parameter 1.0, BN denotes a BatchNorm layer, GN denotes a Gaussian noise regularization layer (active only during training) with default standard deviation 0.5, and FC denotes a fully-connected layer. 10 hidden units are used in all cells, including for the latent space  $L = 10$ , and network architecture or structural hyperparameters are kept the same across experiments. For both architectures, no activation is applied to the layer just before the latent layer, because the shape of the activation function is observed to constrain the range of values in latent space, consistent with observations of other studies (Otto & Rowley, 2019).

## D. Extended description of similarity metrics

**Evaluation metrics.** We introduce several methods for comparing the original system  $Y$  with its reconstruction  $\hat{Y}$ . We emphasize that this comparison does not occur during training (the autoencoder only sees one coordinate); rather, we use these metrics to assess how well our models can reconstruct known systems.

*1. Dimension accuracy.* A basic, informative property of a dynamical system  $\dot{\mathbf{y}}(t)$  is its dimensionality,  $d = \dim(\mathbf{y})$ , the minimum number of distinct variables necessary to fully specify the dynamics. Embeddings with  $d_E < d$  discard

essential information by collapsing independent coordinates, while embeddings with  $d_E > d$  contain redundancy. We thus introduce a measure of embedding parsimony based on the effective number of latent coordinates present in the learned embedding.

We equate the activity of a given latent dimension with its dimension-wise variance  $\text{Var}(\hat{\mathbf{y}})$ , calculated across the ensemble of model inputs  $\{\mathbf{x}_i\}_1^N$ . We compare the distribution of activity in the reconstruction  $\hat{Y}$  to the original attractor  $Y$ , padding the dimensionality of the original attractor with zeros as needed:

$$\mathcal{S}_{dim} = 1 - \frac{||\text{SORT}(\text{Var}(\mathbf{y})) - \text{SORT}(\text{Var}(\hat{\mathbf{y}}))||}{||\text{Var}(\mathbf{y})||}. \quad (\text{A1})$$

This quantity is maximized when the number of active latent dimensions, and their relative activity, matches that found in the original attractor. We further discuss this score, and general properties of the embedding dimension  $d_E$ , in the next section.

**2. Procrustes distance.** Because a univariate measurement cannot contain information about the symmetry group or chirality of the full attractor, when computing pointwise similarity between the true and embedded attractors, we first align the two datasets using the Procrustes transform,

$$P = \arg \min_{\tilde{P}} ||\tilde{P}\hat{Y} - Y||_F \quad \text{s.t.} \quad \tilde{P}^\top \tilde{P} = I,$$

where  $I$  is the identity matrix. This transformation linearly registers the embedded attractor to the original attractor via translation, rotation, reflection, but *not* shear. For example, after this transformation, mirror images of a spiral would become congruent, whereas a sphere and ellipsoid would not. After calculating this transform, we compute the standard Euclidean distance, which we normalize to produce a similarity metric,

$$\mathcal{S}_{proc} = 1 - \frac{||P\hat{Y} - Y||}{||Y - \bar{Y}||}$$

where the mean square error  $||\cdot||^2$  is averaged across the batch, and  $\bar{Y}_k = \sum_{b=1}^N Y_{kb}$ . This metric corresponds to a weighted variant of the classical attractor similarity measure introduced by Diks et al. (1996). In addition to the mean-squared error, we also calculate several other distance measures between  $P\hat{Y}$  and  $Y$ , such as the dynamic time warping distance, the Frechet distance  $\mathcal{S}_{\text{Frech}}$ , and the undirected Hausdorff distance. Due to space constraints, we only include these metrics in the supplementary material; however, the results were largely the same as those for the  $\mathcal{S}_{proc}$ .

**3. Persistent Homology.** The persistence diagram for a point cloud measures the appearance or disappearance of essential topological features as a function of length scale.

A length scale  $\epsilon$  is fixed, and then all points are replaced by  $\epsilon$ -radius balls, the union of which defines a surface. Key topological features (e.g., holes, voids, and extrema) are then measured, the parameter  $\epsilon$  is increased, and the process is repeated. This process produces a birth-death diagram for topological features parametrized by different length scales. We refer to a recent review (Edelsbrunner & Harer, 2008) for further details of the technique. Here, we build upon recent results showing that the "bottleneck distance"  $d_b$  (the shortest accumulated distance) between two persistence diagrams can be used as a measure of topological similarity between the attractors (Venkataraman et al., 2016; Tran & Hasegawa, 2019). We express this quantity as a normalized similarity measure

$$\mathcal{S}_{\text{homol}}(\mathcal{P}_Y, \mathcal{P}_{\hat{Y}}) = 1 - \frac{d_b(\mathcal{P}_Y, \mathcal{P}_{\hat{Y}})}{d_b(\mathcal{P}_Y, 0)}$$

where  $\mathcal{P}_Y, \mathcal{P}_{\hat{Y}}$  denote the persistence diagrams associated with the point clouds  $Y$  and  $\hat{Y}$ , and the denominator denotes distance to a "null" diagram with no salient topological features. Two attractors will have a high bottleneck similarity if they share essential topological features (such as holes, voids, and extrema). We compute birth-death persistence diagrams using the `Ripser` software package (Tralie et al., 2018), and we compute bottleneck distances between diagrams using the `persim` software package.

**4. Local neighbor accuracy.** We seek to quantify whether points on  $\hat{Y}$  are embedded in the same neighborhood as they are on  $Y$ . We pick single datapoints  $\hat{\mathbf{y}}_i$  from the attractor  $\hat{Y}$ , and then regress their expected position  $\tilde{\mathbf{y}}_i$  using the centroid of the set  $\kappa$  of their  $k$  nearest neighbors,  $\tilde{\mathbf{y}}_i = (1/k) \sum_{j \in \{\kappa\}} \hat{\mathbf{y}}_j$ . This "simplex" interpolation method was originally developed to identify noise versus chaos in time series embeddings (Sugihara & May, 1990). We first define the accumulated difference  $C$  between the predicted point location  $\tilde{\mathbf{y}}_i$ , and the location  $\mathbf{y}_{i+\tau}$  observed some time  $\tau$  later,

$$C(\hat{Y}, \tau) = \frac{1}{N - \tau} \frac{\sum_{i=1}^N \sum_{m=1}^L (\hat{Y}_{i+\tau, m} - \tilde{Y}_{i, m})^2}{\sum_{m=1}^L \text{Var}(Y)}$$

where  $\text{Var}(Y) \in \mathbb{R}^L$  denotes the dimension-wise variance across all datapoints. We evaluate this quantity for both  $Y$  and  $\hat{Y}$ , and define a similarity metric,

$$\mathcal{S}_{\text{simp}}(\hat{Y}, Y, \tau) = 1 - \frac{|C(Y, \tau) - C(\hat{Y}, \tau)|}{|1 - C(Y, \tau)|}$$

While  $C$  decreases with  $\tau$  for most time series due to decorrelation,  $\mathcal{S}_{\text{simp}}$  decreases only if the autocorrelation decreases faster than the original attractor. Generally  $\mathcal{S}_{\text{simp}}$  decreases smoothly with  $\tau$ , and so below we report results for the timescale  $\tau = 2T$ , where  $T$  is the width of the Hankel matrix.



5. *Global neighbor coverage.* For the  $i^{\text{th}}$  point of the  $N$  embedded points in  $\hat{Y}$ , we define  $\kappa_i(k)$  as the number  $k$  nearest neighbors that correspond to true neighbors in the original dataset  $Y$ . For example, if the indices of the three closest neighbors to point 1 in  $Y$  are 11, 14, 29 in order of relative distance, whereas its three closest neighbors are 11, 29, 15 in  $\hat{Y}$ , then  $\kappa_1(1) = 1$ ,  $\kappa_1(2) = 1$ ,  $\kappa_1(3) = 2$ . We average this quantity across all points in  $\hat{Y}$ ,  $\bar{\kappa}(k) = \sum_{b=1}^B \kappa_b(k)$ . We note that, for a random shuffling of neighbors,  $\kappa(k)$  is given by the hypergeometric distribution describing a random sample of  $k$  objects from a collection of  $N$  distinct objects without replacement,  $\kappa(k) \sim f(N, N, k)$ ,  $\bar{\kappa}(k) = k^2/N$ ; in contrast, a set of perfectly matching neighbors will exhibit  $\bar{\kappa}(k) = k$ . We use these bounds to define the neighbor similarity as the area under the curve between the observed  $\bar{\kappa}(k)$  and the random case, normalized by the best-case-scenario

$$\mathcal{S}_{\text{nn}} = \sum_k \frac{\bar{\kappa}(k) - k^2/N}{k - k^2/N}$$

Similar to an ROC AUC, this metric depends on the fraction of correct neighbors within the closest  $k$  neighbors, as the parameter  $k$  is swept.

6. *Fractal dimension.* As an example of a physically-informative quantity that can be computed for an attractor, but not a raw time series, we compare the correlation dimension (a type of fractal dimension) of the original attractor  $c_Y$  and its reconstruction  $c_{\hat{Y}}$  using the symmetric mean absolute percent error

$$\mathcal{S}_{\text{corr}}(c_Y, c_{\hat{Y}}) = 1 - \frac{|c_Y - c_{\hat{Y}}|}{|c_Y| + |c_{\hat{Y}}|}.$$

We use the correlation dimension instead of related physical properties (such as the Lyapunov exponent, or Kolmogorov-Sinai entropy) because, unlike other properties, the correlation dimension can be robustly measured in a parameter-free manner, without random subsampling of points, using a popular algorithm by [Grassberger & Procaccia \(1983\)](#).

## E. Additional Experiments

We repeat the experiment in which the regularizer strength  $\lambda$  is varied, and show similar results for both the LSTM and the MLP autoencoders in Figure S1

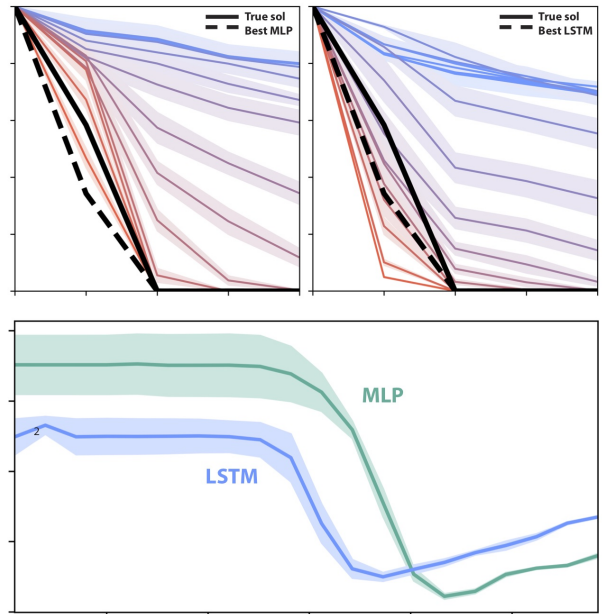


Figure S1. (A) The distribution of normalized latent variances as a function of regularizer strength from  $\lambda = 0$  (blue) to  $\lambda = 0.1$  (red), with the normalized variance for the full solution (solid black line) and for the final best-performing model (dashed black line). (B) The dimensionality error  $1 - \mathcal{S}_{\text{dim}}$  as a function of  $\lambda$ . Error ranges correspond to 5 replicates.

Table S1. Results for five datasets with known attractors. Errors correspond to standard errors over 5 replicates with random initial weights. For each row, the maximum value, as well as any other values with error ranges overlapping the range of the maximum, is marked in bold.

METRIC	ICA	tICA	ETD	MLP	LSTM	MLP-FNN	LSTM-FNN
LORENZ							
$\mathcal{S}_{\text{SIMP}}$	0.384	0.153	0.235	$0.65 \pm 0.06$	$0.63 \pm 0.09$	<b><math>0.8 \pm 0.1</math></b>	$0.68 \pm 0.07$
$\mathcal{S}_{\text{CORR}}$	<b>0.992</b>	<b>0.985</b>	<b>0.978</b>	$0.91 \pm 0.01$	$0.87 \pm 0.02$	<b><math>0.953 \pm 0.009</math></b>	<b><math>0.98 \pm 0.02</math></b>
$\mathcal{S}_{\text{HOMOL}}$	0.049	0.123	<b>0.668</b>	$0.01 \pm 0.01$	$0.04 \pm 0.03$	<b><math>0.47 \pm 0.05</math></b>	$0.3 \pm 0.1$
$\mathcal{S}_{\text{PROC}}$	-0.015	0.037	0.212	$0.09 \pm 0.05$	$0.20 \pm 0.03$	$0.23 \pm 0.08$	<b><math>0.37 \pm 0.02</math></b>
$\mathcal{S}_{\text{DTW}}$	0.237	0.21	0.27	$0.25 \pm 0.04$	$0.31 \pm 0.03$	<b><math>0.39 \pm 0.09</math></b>	<b><math>0.47 \pm 0.03</math></b>
$\mathcal{S}_{\text{NN}}$	0.277	0.296	<b>0.384</b>	$0.25 \pm 0.06$	$0.25 \pm 0.06$	<b><math>0.4 \pm 0.02</math></b>	<b><math>0.4 \pm 0.02</math></b>
$\mathcal{S}_{\text{DIM}}$	0.171	0.394	<b>0.628</b>	$-0.4 \pm 0.1$	$-0.06 \pm 0.08$	<b><math>0.88 \pm 0.02</math></b>	<b><math>0.66 \pm 0.01</math></b>
DOUBLE PENDULUM							
$\mathcal{S}_{\text{SIMP}}$	0.606	0.856	0.51	$0.80 \pm 0.04$	$0.74 \pm 0.04$	$0.89 \pm 0.07$	<b><math>0.98 \pm 0.07</math></b>
$\mathcal{S}_{\text{CORR}}$	0.985	0.861	0.822	$0.96 \pm 0.01$	<b><math>0.966 \pm 0.006</math></b>	$0.951 \pm 0.003$	<b><math>0.986 \pm 0.008</math></b>
$\mathcal{S}_{\text{HOMOL}}$	0.191	0.202	0.176	$0.18 \pm 0.03$	$0.19 \pm 0.02$	<b><math>0.26 \pm 0.03</math></b>	<b><math>0.25 \pm 0.02</math></b>
$\mathcal{S}_{\text{PROC}}$	0.002	0.001	0.003	<b><math>0.013 \pm 0.004</math></b>	$0.008 \pm 0.005$	<b><math>0.013 \pm 0.003</math></b>	<b><math>0.016 \pm 0.006</math></b>
$\mathcal{S}_{\text{DTW}}$	0.026	0.069	<b>0.108</b>	$0.11 \pm 0.02$	$0.11 \pm 0.01$	<b><math>0.136 \pm 0.009</math></b>	<b><math>0.132 \pm 0.008</math></b>
$\mathcal{S}_{\text{NN}}$	0.019	0.031	0.055	$0.041 \pm 0.003$	$0.042 \pm 0.002$	$0.05 \pm 0.001$	<b><math>0.060 \pm 0.001</math></b>
$\mathcal{S}_{\text{DIM}}$	-1.772	-1.914	0.927	$-0.6 \pm 0.2$	$-0.8 \pm 0.3$	$0.801 \pm 0.006$	<b><math>0.97 \pm 0.01</math></b>
ECOSYSTEM							
$\mathcal{S}_{\text{SIMP}}$	0.608	0.628	0.619	$0.83 \pm 0.01$	<b><math>0.85 \pm 0.008</math></b>	<b><math>0.84 \pm 0.03</math></b>	<b><math>0.87 \pm 0.02</math></b>
$\mathcal{S}_{\text{CORR}}$	0.856	<b>0.890</b>	0.820	$0.876 \pm 0.004$	$0.877 \pm 0.004$	<b><math>0.904 \pm 0.009</math></b>	<b><math>0.888 \pm 0.003</math></b>
$\mathcal{S}_{\text{HOMOL}}$	0.185	0.066	0.256	$0.17 \pm 0.03$	$0.09 \pm 0.04$	<b><math>0.36 \pm 0.03</math></b>	<b><math>0.33 \pm 0.03</math></b>
$\mathcal{S}_{\text{PROC}}$	<b>0.055</b>	0.024	0.025	$-0.01 \pm 0.03$	$-0.1 \pm 0.05$	<b><math>0.04 \pm 0.03</math></b>	<b><math>0.08 \pm 0.05</math></b>
$\mathcal{S}_{\text{DTW}}$	0.111	0.115	0.051	<b><math>0.11 \pm 0.02</math></b>	$0.05 \pm 0.03$	<b><math>0.12 \pm 0.02</math></b>	<b><math>0.15 \pm 0.03</math></b>
$\mathcal{S}_{\text{NN}}$	0.133	0.133	0.146	$0.304 \pm 0.005$	$0.304 \pm 0.004$	$0.30 \pm 0.03$	<b><math>0.313 \pm 0.005</math></b>
$\mathcal{S}_{\text{DIM}}$	-0.882	0.60	0.664	$0.38 \pm 0.08$	$0.51 \pm 0.05$	<b><math>0.90 \pm 0.02</math></b>	<b><math>0.92 \pm 0.02</math></b>
TORUS							
$\mathcal{S}_{\text{SIMP}}$	0.651	0.219	0.361	$0.55 \pm 0.06$	$0.65 \pm 0.03$	$0.56 \pm 0.07$	<b><math>0.68 \pm 0.01</math></b>
$\mathcal{S}_{\text{CORR}}$	<b>0.994</b>	0.952	<b>0.993</b>	$0.982 \pm 0.006$	$0.87 \pm 0.03$	<b><math>0.994 \pm 0.004</math></b>	<b><math>0.99 \pm 0.01</math></b>
$\mathcal{S}_{\text{HOMOL}}$	0.001	-1.442	-0.827	$-0.6 \pm 0.06$	$-0.4 \pm 0.2$	$-0.3 \pm 0.2$	<b><math>0.33 \pm 0.09</math></b>
$\mathcal{S}_{\text{PROC}}$	0.157	-0.102	-0.008	$0.1 \pm 0.1$	$-0.07 \pm 0.08$	<b><math>0.4 \pm 0.1</math></b>	<b><math>0.4 \pm 0.1</math></b>
$\mathcal{S}_{\text{DTW}}$	0.403	0.292	<b>0.586</b>	$0.24 \pm 0.07$	$0.19 \pm 0.07$	<b><math>0.60 \pm 0.08</math></b>	<b><math>0.50 \pm 0.09</math></b>
$\mathcal{S}_{\text{NN}}$	0.269	0.194	<b>0.444</b>	$0.28 \pm 0.03$	$0.28 \pm 0.01$	<b><math>0.42 \pm 0.01</math></b>	<b><math>0.45 \pm 0.02</math></b>
$\mathcal{S}_{\text{DIM}}$	-0.619	-0.652	0.722	$0.1 \pm 0.1$	$-0.3 \pm 0.3$	<b><math>0.96 \pm 0.04</math></b>	$0.71 \pm 0.01$
RÖSSLER							
$\mathcal{S}_{\text{SIMP}}$	0.506	0.914	<b>0.969</b>	$0.88 \pm 0.02$	$0.85 \pm 0.05$	$0.90 \pm 0.03$	<b><math>0.93 \pm 0.04</math></b>
$\mathcal{S}_{\text{CORR}}$	0.771	0.994	<b>0.999</b>	$0.94 \pm 0.02$	$0.87 \pm 0.03$	$0.985 \pm 0.003$	<b><math>0.996 \pm 0.001</math></b>
$\mathcal{S}_{\text{HOMOL}}$	0.001	0.06	<b>0.501</b>	$0.08 \pm 0.04$	$0.08 \pm 0.07$	$0.27 \pm 0.04$	$0.32 \pm 0.05$
$\mathcal{S}_{\text{PROC}}$	0.123	-0.002	0.027	$0.01 \pm 0.09$	<b><math>0.33 \pm 0.04</math></b>	<b><math>0.3 \pm 0.1</math></b>	<b><math>0.28 \pm 0.06</math></b>
$\mathcal{S}_{\text{DTW}}$	0.351	0.547	0.527	$0.23 \pm 0.07$	$0.43 \pm 0.05$	<b><math>0.52 \pm 0.09</math></b>	<b><math>0.64 \pm 0.03</math></b>
$\mathcal{S}_{\text{NN}}$	0.332	<b>0.742</b>	<b>0.762</b>	$0.43 \pm 0.03$	$0.42 \pm 0.03$	$0.64 \pm 0.01$	<b><math>0.72 \pm 0.03</math></b>
$\mathcal{S}_{\text{DIM}}$	-0.48	0.423	<b>0.727</b>	$0.64 \pm 0.04$	$0.5 \pm 0.1$	<b><math>0.694 \pm 0.05</math></b>	<b><math>0.675 \pm 0.06</math></b>

## References

- Abadi, M., Barham, P., Chen, J., Chen, Z., Davis, A., Dean, J., Devin, M., Ghemawat, S., Irving, G., Isard, M., et al. Tensorflow: A system for large-scale machine learning. In *12th {USENIX} Symposium on Operating Systems Design and Implementation ({OSDI} 16)*, pp. 265–283, 2016.
- Abarbanel, H. D., Brown, R., Sidorowich, J. J., and Tsimring, L. S. The analysis of observed chaotic data in physical systems. *Reviews of modern physics*, 65(4):1331, 1993.
- Asseman, A., Kornuta, T., and Ozcan, A. Learning beyond simulated physics. In *NIPS Modeling and Decision-making in the Spatiotemporal Domain Workshop*, 2018.
- Bar-Sinai, Y., Hoyer, S., Hickey, J., and Brenner, M. P. Learning data-driven discretizations for partial differential equations. *Proceedings of the National Academy of Sciences*, 116(31):15344–15349, 2019.
- Broomhead, D. S. and Jones, R. Time-series analysis. *Proceedings of the Royal Society of London. A. Mathematical and Physical Sciences*, 423(1864):103–121, 1989.
- Brunton, S. L., Brunton, B. W., Proctor, J. L., Kaiser, E., and Kutz, J. N. Chaos as an intermittently forced linear system. *Nature communications*, 8(1):19, 2017.
- Cao, L. Practical method for determining the minimum embedding dimension of a scalar time series. *Physica D: Nonlinear Phenomena*, 110(1-2):43–50, 1997.
- Champion, K., Lusch, B., Kutz, J. N., and Brunton, S. L. Data-driven discovery of coordinates and governing equations. *Proceedings of the National Academy of Sciences*, 116(45):22445–22451, 2019.
- Chaudhuri, R., Gerçek, B., Pandey, B., Peyrache, A., and Fiete, I. The intrinsic attractor manifold and population dynamics of a canonical cognitive circuit across waking and sleep. *Nature neuroscience*, 22(9):1512–1520, 2019.
- Clark, T. and Luis, A. D. Nonlinear population dynamics are ubiquitous in animals. *Nature Ecology & Evolution*, 4(1):75–81, 2020.
- Cobey, S. and Baskerville, E. B. Limits to causal inference with state-space reconstruction for infectious disease. *PloS one*, 11(12), 2016.
- Cogswell, M., Ahmed, F., Girshick, R., Zitnick, L., and Batra, D. Reducing overfitting in deep networks by decorrelating representations. In *International Conference on Learning Representations*, pp. 1–12, 2016.
- Costa, A. C., Ahamed, T., and Stephens, G. J. Adaptive, locally linear models of complex dynamics. *Proceedings of the National Academy of Sciences*, 116(5):1501–1510, 2019.
- Deyle, E. R. and Sugihara, G. Generalized theorems for nonlinear state space reconstruction. *PLoS One*, 6(3), 2011.
- Dhir, N., Kosiorek, A. R., and Posner, I. Bayesian delay embeddings for dynamical systems. In *NIPS Timeseries Workshop*, 2017.
- Diks, C., Van Zwet, W., Takens, F., and DeGoede, J. Detecting differences between delay vector distributions. *Physical Review E*, 53(3):2169, 1996.
- Dua, D. and Graff, C. UCI machine learning repository, 2017. URL <http://archive.ics.uci.edu/ml>.
- Edelsbrunner, H. and Harer, J. Persistent homology—a survey. *Contemporary mathematics*, 453:257–282, 2008.
- Erem, B., Orellana, R. M., Hyde, D. E., Peters, J. M., Duffy, F. H., Stovicek, P., Warfield, S. K., MacLeod, R. S., Tadmor, G., and Brooks, D. H. Extensions to a manifold learning framework for time-series analysis on dynamic manifolds in bioelectric signals. *Physical Review E*, 93(4):042218, 2016.
- Fraser, A. M. and Swinney, H. L. Independent coordinates for strange attractors from mutual information. *Physical review A*, 33(2):1134, 1986.
- Garcia, S. P. and Almeida, J. S. Multivariate phase space reconstruction by nearest neighbor embedding with different time delays. *Physical Review E*, 72(2):027205, 2005.
- Giannakis, D. and Majda, A. J. Nonlinear laplacian spectral analysis for time series with intermittency and low-frequency variability. *Proceedings of the National Academy of Sciences*, 109(7):2222–2227, 2012.
- Goldberger, A. L., Amaral, L. A., Glass, L., Hausdorff, J. M., Ivanov, P. C., Mark, R. G., Mietus, J. E., Moody, G. B., Peng, C.-K., and Stanley, H. E. Physiobank, physiokit, and physionet: components of a new research resource for complex physiologic signals. *Circulation*, 101(23):e215–e220, 2000.
- Grassberger, P. and Procaccia, I. Measuring the strangeness of strange attractors. *Physica D: Nonlinear Phenomena*, 9(1-2):189–208, 1983.
- Han, M., Feng, S., Chen, C. P., Xu, M., and Qiu, T. Structured manifold broad learning system: a manifold perspective for large-scale chaotic time series analysis and

- prediction. *IEEE Transactions on Knowledge and Data Engineering*, 2018.
- Harrigan, M. P., Sultan, M. M., Hernández, C. X., Husic, B. E., Eastman, P., Schwantes, C. R., Beauchamp, K. A., McGibbon, R. T., and Pande, V. S. Msmbuilder: statistical models for biomolecular dynamics. *Biophysical journal*, 112(1):10–15, 2017.
- Huisman, J. and Weissing, F. J. Biodiversity of plankton by species oscillations and chaos. *Nature*, 402(6760):407, 1999.
- Jiang, H. and He, H. State space reconstruction from noisy nonlinear time series: An autoencoder-based approach. In *2017 International Joint Conference on Neural Networks (IJCNN)*, pp. 3191–3198. IEEE, 2017.
- Juang, J.-N. and Pappa, R. S. An eigensystem realization algorithm for modal parameter identification and model reduction. *Journal of guidance, control, and dynamics*, 8(5):620–627, 1985.
- Kaplan, D. T. and Cohen, R. J. Is fibrillation chaos? *Circulation Research*, 67(4):886–892, 1990.
- Kennel, M. B., Brown, R., and Abarbanel, H. D. Determining embedding dimension for phase-space reconstruction using a geometrical construction. *Physical review A*, 45(6):3403, 1992.
- Laguna, P., Mark, R. G., Goldberg, A., and Moody, G. B. A database for evaluation of algorithms for measurement of qt and other waveform intervals in the ecg. In *Computers in cardiology 1997*, pp. 673–676. IEEE, 1997.
- Linderman, S., Johnson, M., Miller, A., Adams, R., Blei, D., and Paninski, L. Bayesian learning and inference in recurrent switching linear dynamical systems. In *Artificial Intelligence and Statistics*, pp. 914–922, 2017.
- Lu, Z., Hunt, B. R., and Ott, E. Attractor reconstruction by machine learning. *Chaos: An Interdisciplinary Journal of Nonlinear Science*, 28(6):061104, 2018.
- Mardt, A., Pasquali, L., Wu, H., and Noé, F. Vampnets for deep learning of molecular kinetics. *Nature communications*, 9(1):5, 2018.
- Nicholl, M. J., Wheatcraft, S. W., Tyler, S. W., and Berkowitz, B. Is old faithful a strange attractor? *Journal of Geophysical Research: Solid Earth*, 99(B3):4495–4503, 1994.
- Otto, S. E. and Rowley, C. W. Linearly recurrent autoencoder networks for learning dynamics. *SIAM Journal on Applied Dynamical Systems*, 18(1):558–593, 2019.
- Pecora, L. M., Moniz, L., Nichols, J., and Carroll, T. L. A unified approach to attractor reconstruction. *Chaos: An Interdisciplinary Journal of Nonlinear Science*, 17(1):013110, 2007.
- Pedregosa, F., Varoquaux, G., Gramfort, A., Michel, V., Thirion, B., Grisel, O., Blondel, M., Prettenhofer, P., Weiss, R., Dubourg, V., et al. Scikit-learn: Machine learning in python. *Journal of machine learning research*, 12(Oct):2825–2830, 2011.
- Pérez-Hernández, G., Paul, F., Giorgino, T., De Fabritiis, G., and Noé, F. Identification of slow molecular order parameters for markov model construction. *The Journal of chemical physics*, 139(1):07B604.1, 2013.
- Rangapuram, S. S., Seeger, M. W., Gasthaus, J., Stella, L., Wang, Y., and Januschowski, T. Deep state space models for time series forecasting. In *Advances in neural information processing systems*, pp. 7785–7794, 2018.
- She, Q., Gao, Y., Xu, K., and Chan, R. H. Reduced-rank linear dynamical systems. In *Thirty-Second AAAI Conference on Artificial Intelligence*, 2018.
- Sugihara, G. and May, R. M. Nonlinear forecasting as a way of distinguishing chaos from measurement error in time series. *Nature*, 344(6268):734–741, 1990.
- Sugihara, G., May, R., Ye, H., Hsieh, C.-h., Deyle, E., Fogarty, M., and Munch, S. Detecting causality in complex ecosystems. *science*, 338(6106):496–500, 2012.
- Sun, Y., Duan, Y., Gong, H., and Wang, M. Learning low-dimensional state embeddings and metastable clusters from time series data. In *Advances in Neural Information Processing Systems*, pp. 4563–4572, 2019.
- Takeishi, N., Kawahara, Y., and Yairi, T. Learning koopman invariant subspaces for dynamic mode decomposition. In *Advances in Neural Information Processing Systems*, pp. 1130–1140, 2017.
- Takens, F. Detecting strange attractors in turbulence. In *Dynamical systems and turbulence, Warwick 1980*, pp. 366–381. Springer, 1981.
- Tralie, C., Saul, N., and Bar-On, R. Ripser.py: A lean persistent homology library for python. *The Journal of Open Source Software*, 3(29):925, Sep 2018. doi: 10.21105/joss.00925. URL <https://doi.org/10.21105/joss.00925>.
- Tran, Q. H. and Hasegawa, Y. Topological time-series analysis with delay-variant embedding. *Physical Review E*, 99(3):032209, 2019.



Venkataraman, V., Ramamurthy, K. N., and Turaga, P. Persistent homology of attractors for action recognition. In *2016 IEEE international conference on image processing (ICIP)*, pp. 4150–4154. IEEE, 2016.

Virtanen, P., Gommers, R., Oliphant, T. E., Haberland, M., Reddy, T., Cournapeau, D., Burovski, E., Peterson, P., Weckesser, W., Bright, J., et al. Scipy 1.0: fundamental algorithms for scientific computing in python. *Nature Methods*, 2020.